Treatment of industrial etching terminal wastewater using $ZnFe_2O_4$/g-C_3N_4 heterojunctions photo-assisted cathodes in single-chamber microbial electrolysis cells

Liping Huang [a],[*], Weifeng Kong [a], Shiping Song [a], Xie Quan [a], Gianluca Li Puma [b],[*]

[a] *Key Laboratory of Industrial Ecology and Environmental Engineering, Ministry of Education (MOE), School of Environmental Science and Technology, Dalian University of Technology, Dalian 116024, China*
[b] *Environmental Nanocatalysis & Photoreaction Engineering, Department of Chemical Engineering, Loughborough University, Loughborough LE11 3TU, United Kingdom*

ARTICLE INFO

ABSTRACT

Cost-effective, semiconductor $ZnFe_2O_4$/g-C_3N_4 heterojunction cathodes were investigated to achieve efficient treatment of industrial etching terminal wastewater in photo-assisted, single-chamber, microbial electrolysis cells (PS-MECs). The PS-MECs performance progressively increased over time, reaching significant Ni(II) removal (4.4 mg/L/h), recalcitrant organics mineralization (11.3 mg/L/h), hydrogen production (0.55 m^3/m^3/d) and solar-to-hydrogen conversion efficiency (6.7%) after 12 days fed-batch operation. The progressive deposition of Ni over the cathodes and the physiological release of extracellular polymeric substances (EPS) dynamically influenced the proportions of reactive oxidative species. Triplet ^{3}EPS* (78%) on both electrodes and cathodic holes (22%) contributed to recalcitrant organics mineralization during the 12th fed-batch operational cycle, while cathodic holes (65%) exceeded anodic ^{3}EPS* (35%) during the 1st-cycle. Significantly different bacterial communities were observed over the cathodes (*Acinetobacter* (17.7%) and *Staphylococcus* (16.8%) and anodes (*Novosphingobium* (42.9%)) after the 12th-cycle, as confirmed by KEGG PICRUSt analysis. This study broadens the application of cost-effective PS-MECs for industrial wastewater treatment.

1. Introduction

Microbial electrolysis cells (MECs) using a small driving force (potential or electricity supply) comprising oxidation of organics by exoelectrogens at the anode and reduction of oxidative substrates by electrotrophs at the cathode, has recently gained tremendous attention for the potential treatment of industrial wastewater [1–3]. Such process may allow the removal/recovery of heavy metals and the simultaneous production of H_2 on the cathode from the energy gained by the oxidation of organics at the anode. Among the proposed MECs designs, the simultaneous treatment of heavy metals and organics is more conveniently carried out in single-chamber MECs rather than in dual-chamber configurations due to simpler architecture, cost-effectiveness, lower internal resistance and easier maintenance [3,4]. The redox process in the photo-assisted single-chamber MECs (PS-MECs) is accelerated by the excitation of semiconductor photocatalysts (e.g., Ni foam/g-C_3N_4/-BiOBr, MoS_2/Cu_2O and CdS/g-C_3N_4) deposited over the anode/cathode with sunlight, producing reductive exited electrons (H_2 production or

organics reduction) and oxidizing holes (organics oxidation) (Table S1) [5–8]. The efficiency and the environmental impact of present systems, however, is limited by the use of semiconductor materials containing undesirable toxic metals such as Cd, Cu and Ni, which can be completely dissolved after prolonged operation [8]. Therefore, it is highly desirable that the next generation of PS-MECs should be developed employing environmentally friendly semiconductors photocatalysts.

In parallel, technological development of the PS-MECs requires experimentation with treatment of complex and real wastewaters rather than single model contaminants [8–10]. Currently, studies in PS-MECs have been limited to the treatment of individual recalcitrant organics (Table S1). Recently, the treatment of real circuit boards etching terminal wastewater (ETW) containing complex recalcitrant organics and heavy metals, has been demonstrated using dual-chamber MECs incorporating photo-assisted abiotic WO_3/MoO_3/g-C_3N_4 cathodes [9,10] or single-chamber MECs without light irradiation [11]. However, the efficiency of the ETW treatment process in these systems was rather low (recalcitrant organics mineralization: 1.10 – 11.6 mg/L/h; Ni(II)

---

* Corresponding authors.
E-mail addresses: lipinghuang@dlut.edu.cn (L. Huang), g.lipuma@lboro.ac.uk (G. Li Puma).

removal: 0.12 – 3.03 mg/L/h; hydrogen production: 0.009 – 0.046 $m^3/m^3/d$), thus the treatment process efficiency needs to be increased to make it industrially viable [9–11]. Moreover, an operational time of 144 h performed in dual-chamber MECs incorporating photo-assisted abiotic $WO_3/MoO_3/g$-C_3N_4 cathodes [9,10] convincingly demonstrated the system robustness over an extended operational time. Although the oxidation of recalcitrant organics in photo-assisted bioelectrochemical systems incorporating W and Mo oxides over cathodes has been accelerated by the production of reactive radical species under irradiation [12–14], many inexpensive Ni-based photocatalysts can also act as potential redox mediators offering additional electron highway that can boost electronic conductivity in electrochemical processes [15–17]. Other key aspects that affect the PS-MECs process performance include the migration of bacteria among anode and cathode and the impact of photo-excited triplet extracellular polymeric substances ($^3EPS^*$) predominantly contributing to photodegradation of single recalcitrant organics [18–20], and these need to be elucidated.

For these reasons, this study demonstrates the treatment of a real ETW effluent, meeting the Chinese wastewater discharge standard (GB25467–2010), over multiple batch cycles operation in single-chamber MECs comprising $ZnFe_2O_4/g$-C_3N_4 photocathodes and graphite felt bioanodes. Coupling $ZnFe_2O_4$ and g-C_3N_4 semiconductor has been proven to form a sustainable and cost-effective catalytic heterojunction for the degradation of single organics species, for heavy metals removal or hydrogen production in conventional abiotic photocatalytic processes, without the dynamic assessment of the process mechanisms (Table S2) [21–23]. Thus, this study, clarifies the impact of the dynamic deposition of heavy metals (e,g., Ni) over the cathode surfaces during the treatment process combined with the temporal electrotrophic and exoelectrogenic physiological release of EPS, which in turn affect the proportions of reactive oxidative species (e.g., triplet active species $^3EPS^*$ and holes) over multiple treatment cycles leading to recalcitrant ETW organics mineralization. Overall, this study makes significant progress on the application of cost-effective and efficient $ZnFe_2O_4/g$-C_3N_4 semiconducting heterojunctions cathodes in PS-MECs for the treatment of actual industrial wastewaters such as ETW.

2. Materials and methods

2.1. Industrial ETW

The main properties of the ETW effluent collected from a storage tank of the company TOTO Ltd. (Dalian, China) are shown in Table 1. The ETW effluent met the China wastewater discharge standards (GB25467–2010) except for the levels of Ni(II) and dissolved organics. The organic matters in the ETW were identified by high performance liquid chromatograph with an APCI (−) ion trap mass spectrometer (Agilent HPLC – MS 6410) and were made primarily by 2-naphthalene-sulfonic acid formaldehyde polymer sodium salt and triethanolamine oleic soap [9–11] which are common species used in metal-working fluids [24,25]. The mineralization of these recalcitrant organics was measured as dissolved COD using the effective manganese method [9–11].

2.2. Synthesis of $ZnFe_2O_4/g$-C_3N_4, and preparation of $ZnFe_2O_4/g$-C_3N_4 photocathode

The synthesis of $ZnFe_2O_4/g$-C_3N_4 and the immobilization of the $ZnFe_2O_4/g$-C_3N_4 on photocathodes were described and provided in Supporting Information (SI). Photoluminescence measurement, UV–vis DRS spectra, Mott-Schottky curves, and XRD and SEM-EDS characterizations are described in SI.

2.3. Reactor, inoculation, and reactor operation

PS-MECs (3.0 cm in diameter and 4.0 cm in length) with a net working volume of 26 mL were used in all experiments. The graphite felt (2.0 cm × 2.0 cm × 0.25 cm, Sanye Co., Beijing, China) anode/cathode supports were previously treated with 32% HCl and then in 35% NaOH [26,27]. The anode was routinely enriched and acclimatized as previously described [26,28]. The bioanode was installed with the $ZnFe_2O_4/g$-C_3N_4 graphite felt cathode (prepared and described in SI) to make up a PC-MEC with an insert of a glass tube (inner diameter: 8 mm) and producing a headspace of 12 mL above the electrolyte. Industrial ETW was used as electrolyte after deoxygenation by sparging nitrogen for 20 min. Unless otherwise stated, each operational cycle lasted 24 h prior to sampling for analyses. The applied voltage to the external circuit of the cell (0.6 V) was provided by a power source (Leici, Shanghai), by connecting the negative lead to the cathode through a 10 Ω resistor for current measurements, and the positive lead to the anode [4,27]. Saturated calomel reference electrodes (241 mV, vs. standard hydrogen electrode, SHE) were used to monitor the electrode potentials, with all potentials reported here vs. SHE. The reactor was irradiated with a 100 W iodine tungsten lamp at 26.9 kLux [12,13]. The lamp was refrigerated by a cooling-fan and the reactors were surrounded by a jacket within which a continuous circulation of water maintained the reactor temperature at 25 ± 3 °C [12,13].

To explore the contribution of different reactive species in the mineralization of recalcitrant organics, sorbic acid (0.2 mM), isopropanol (0.5 mM) and KI (10 mM) were added respectively to the reactors to selectively quench $^3EPS^*$, ·OH and holes [8,9,18,29].

A total of 12 fed-batch anaerobic cycles were carried out corresponding to 288 h continuous operation. Anodes and cathodes were sampled for SEM-EDS characterization, electrochemical analysis, and EPS determination at the end of the 1st, the 6th and of the 12th cycle. The abiotic $ZnFe_2O_4/g$-C_3N_4 graphite felt heterojunction cathode was initially installed with a well-acclimated graphite felt bioanode, however, its properties were progressively altered over time. Therefore, the cathodic holes always referred to the holes generated by the $ZnFe_2O_4/g$-C_3N_4 heterojunction cathode, whereas the $^3EPS^*$ was reasonably ascribed to the bacterial communities developed on both electrodes over time. Considering the impact of calcination on the activity of the deposited nickel in pure photocatalysis or electrochemical processes [15,17], the 6-cycle operated cathodes were specifically disassembled from the reactors and calcined at 550 °C for 2 h with a heating rate of 4 °C/min. These calcinated cathodes subsequently assembled back to the reactors, were then operated for another 6 cycles to assess system performance.

Control experiments under open circuit conditions (OCCs, single bio-light-irradiation processes) were performed to examine the role of circuital current on system performance, whereas the experiments operated under darkness (individual bioelectrochemical processes) reflected the impact of light irradiation on system performance. The single-chamber MECs operated under both darkness and OCC reflected the roles of both light irradiation and circuital current on system performance. The abiotic controls implied the absence of both exoelectrogens and electrotrophs on system performance. Reactors operated under darkness and abiotic conditions reflected the role of light irradiation and biotic catalysis on system performance, whereas those performed under OCC and abiotic conditions, implied the impact of

Table 1
Composition of actual etching terminal wastewater.

Parameter	Value	Parameter	Value
Organics (SCOD)	330 ± 1 mg/L	sulfide	0.7 ± 0.1
Ni(II)	106 ± 2 mg/L	SO_4^{2-}	4.3 ± 0.1
NH_4^+ − N	6.6 ± 0.2 mg/L	total chlorine	0.5 ± 0.1
NO_3^- − N	3.3 ± 0.1 mg/L	pH	5.43 ± 0.01
NO_2^- − N	0.1 ± 0.0 mg/L	conductivity	9.80 ± 1.30 mS/cm

circuital current and biotic catalysis on system performance. Those performed with abiotic, OCC and under darkness, reflected the role of light irradiation, circuital current and biocatalysts on system performance.

2.4. Sampling, analyses and characterizations

The hydrogen evolved in the headspace of each PS-MEC was measured using a gas chromatograph (GC7900, Tianmei, Shanghai) and a molecular sieve column (TDX-01, 60 – 80, 4 mm × 2 m) with argon as the carrier gas. The mineralization of recalcitrant organics in the effluents were assessed by measuring the dissolved COD using the manganese method which proved to be a reliable method, after previous filtration of the liquid samples using a 0.22 μm membrane (Sangon Biotech, Shanghai) [9–11,30]. Leached Fe and Zn in the electrolyte was determined by atomic absorption spectroscopy (AAnalyst 700, PerkinElmer).

The extraction of EPS from either the anode after the 1st operational cycle or from both electrodes after the 6th or 12th operational cycles, was performed as previously reported [31]. The amount of exopolysaccharides in the EPS were determined by the phenol-sulfuric acid method [32], whereas the corresponding exoproteins were measured by the Bradford assay (Bio-Rad, Hercules, CA) using bovine serum albumin as calibration standard.

Both CV and EIS were performed using the same potentiostat (VSP, BioLogic, France) with a three-electrode system comprising a working electrode (e.g., cathode or anode electrodes), a Pt foil (2 × 4 cm) counter electrode, and a saturated calomel reference electrode (0.24 V, vs. SHE) located 1 cm away from the working electrode [27]. CV performed at a range of 0.3 – 1.1 V with a scan rate of 0.1 mV/s. DPV, as described by Okamoto et al. [33], was further used to assess the likely change of outer membrane *c*-type cytochromes of the PS-MECs. EIS was conducted under the electrode open circuital conditions, over a frequency range of 100 kHz – 10 mHz with a sinusoidal perturbation of 10 mV amplitude. The equivalent circuit and detailed value of different resistances were obtained through Zsimpwin software.

A SEM (Nova NanoSEM 450, FEI company, USA) equipped with an EDS (X-MAX 20 – 50 mm^2, Oxford Instruments, UK) was used to examine the morphologies of both electrodes and quantify the elemental composition.

After the 12th operational cycle, both the anodes and the cathodes of duplicate single-chamber reactors in the presence or in the absence of light illumination were collected and mixed to analyze the bacterial community using 16 S rRNA technology (SI) [11,34,35]. The taxonomies for 16 S rRNA genes obtained were deposited in the NCBI SRA (http://www.ncbi.nlm.nih.gov/sra) with the BioProject ID of PRJNA851187.

PICRUSt enabling the function prediction of uncultivated microbes and applicable in detecting the 16 S rRNA marker gene sequences of bacterial and archaeal genomes, was used to establish the direct evidence of microbial communities' functional capabilities [36]. The KEGG based PICRUSt analysis was conducted to give comprehensive information concerning the microbial functional genes expressions after performing BLASTP according to KEGG (http://www.genome.jp/kegg/).

2.5. Calculations

The hydrogen production (m^3/m^3/d) was calculated as previously described [27,34]. Circuital current was normalized to the projected surface area of the cathode, allowing the comparison of the results to literature studies on photo-assisted MESs (Table S1).

The coulombic efficiency in terms of Ni(II) reduction (CE_{Ni}, %) or hydrogen production (CE_{H2}, %), and the energy efficiencies for either Ni (II) reduction or hydrogen evolution relative to the added substrate ($\eta_{s,Ni}$ or $\eta_{s,H2}$, %), for the electrical input ($\eta_{E,Ni}$ or $\eta_{E,H2}$, %), or for both the electricity and substrate inputs ($\eta_{s+E,Ni}$ or $\eta_{s+E,H2}$, %), were calculated

according to Eqs. S1 – S8 [6], whereas the solar-to-hydrogen conversion efficiency (η_L, %) was calculated from Eq. S9 [8].

The values reported were averaged based on the statistics analysis of three replicate experiments for each of the duplicate reactors. One-way ANOVA in SPSS 19.0 was used to analyze the statistical differences among the data at significance levels of $p < 0.05$.

3. Results and discussion

3.1. Electrodes characterization

The characterization of the prepared ZnFe$_2$O$_4$/g-C$_3$N$_4$ graphite felt photocathode by UV–vis DRS, XRD, PL, photo-current, SEM-EDS, CV and EIS, as well as the tuning of electrode composition and loading were provided in SI, and shown in Fig. S1, Fig. S2, and Table S3 [35]. The anodic bacterial community composition routinely acclimatized were provided in Fig. S3.

3.2. System performance

Simultaneous removal of Ni(II) (4.4 ± 0.0 mg/L/h), recalcitrant organics mineralization (9.7 ± 0.2 mg/L/h) (Fig. 1A) and hydrogen production (0.43 ± 0.02 m^3/m^3/d) at a circuital current of 3.3 ± 0.0 A/m^2 (Fig. 1B) was achieved after an operational time of 24 h. These results were significantly higher than the rate values recorded with the controls, in the absence of light irradiation or/and circuital current, or in the abiotic controls (Fig. 1A and B). This demonstrated the tremendous importance of light irradiation, circuital current and bioanodic catalyst nature on the efficiency of ETW treatment in PS-MEC systems. The reactor effluent after 24 h treatment (SCOD: 97.6 ± 3.8 mg/L, Ni(II): 0.4 mg/L, sulfide: 0.5 ± 0.1 mg/L, NO$_3^-$-N: 0.7 ± 0.2 mg/L, NO$_2^-$-N: 0.1 ± 0.1 mg/L, NO$_4^-$-N: 3.1 ± 0.2 mg/L and total chlorine: 0.5 ± 0.0 mg/L) met the China national discharge standards (GB25467–2010), while 12 h treatment proved to be insufficient (Fig. S4). Comparing the performance of the PS-MECs with that using a single-chamber MECs without catalyst and irradiation [11], the increase in performance was 8.8-fold (organic mineralization), 36.7-time (Ni(II) removal) and 46-fold (hydrogen production), while it was 3.2-fold increase (Ni(II) removal) and alike organics mineralization (7.0 – 11.6 mg/L/h) in comparison to the treatment in photo-assisted WO$_3$/MoO$_3$/g-C$_3$N$_4$ abiotic cathode dual-chamber MECs [9,10]. Overall, these results demonstrate the significant benefit of utilizing a single rather than dual-chamber photo-assisted MECs to achieve efficient ETW treatment. The removal of Ni(II) in this system also compared with the removal (4.6 mg/L/h) achieved using abiotic cathodes in dual-chamber MECs without light irradiation at an applied voltage of 1.0 V, at an initial Ni(II) concentration of 295 mg/L and at a more acidic pH of 2.85 [37]. Higher applied voltages and initial Ni(II) concentrations, and more acidic pH generally favors Ni(II) removal by abiotic cathodes in dual-chamber MECs [1,37]. Collectively these results demonstrated the benefits of using ZnFe$_2$O$_4$/g-C$_3$N$_4$ photocathode single-chamber MECs for efficient ETW treatment.

The higher circuital current under light irradiation invariably contributed to achieving higher CE_{Ni} and CE_{H2} (Fig. 1C), as well as higher energy efficiencies ($\eta_{s,Ni}$, $\eta_{s,H2}$, $\eta_{E,Ni}$, and $\eta_{E,H2}$) (Fig. 1D and E) with a substantially high solar-to-hydrogen conversion efficiency of 5.3 ± 0.3% (Fig. 1F). The value of $\eta_{E,H2}$ of 204 ± 2% significantly higher than 100% indicated a positive energy feedback in the ETW treatment, which gives a technology advantage over other energy demanding conventional ETW treatment processes, such as electrochemical or biological processes [24,25]. The competitive advantage extends also over that of newly developed pure single-chamber MECs [11] or photo-assisted WO$_3$/MoO$_3$/g-C$_3$N$_4$ abiotic cathode dual-chamber MECs [9] which required a net input of external energy. The solar-to-hydrogen conversion efficiency was also appreciably higher than the 0.12% obtained with a MoS$_2$/Cu$_2$O photocathode single-chamber MECs, fed with acetate as a fuel, and at the same applied voltage of 0.6 V (Table S1) [6],
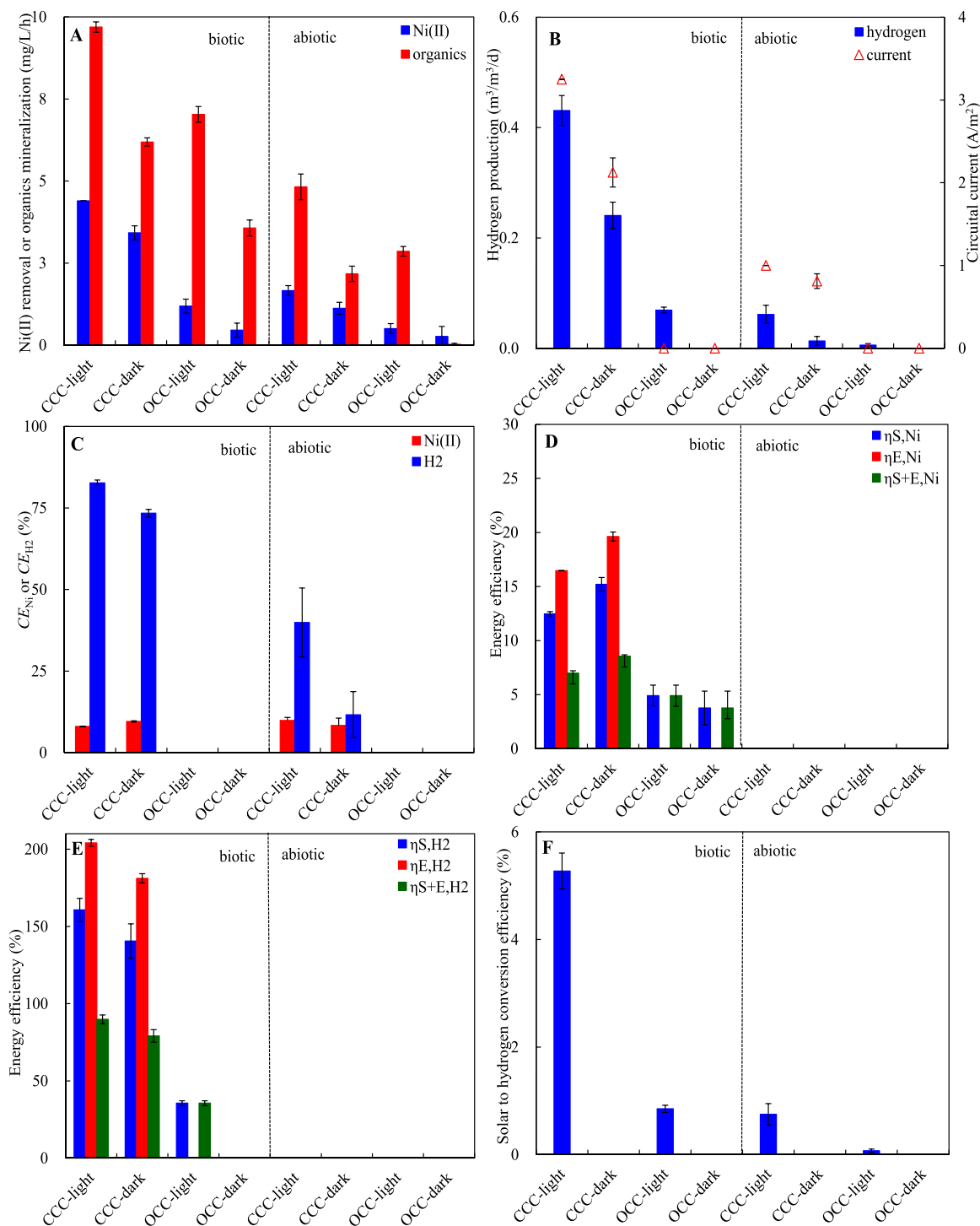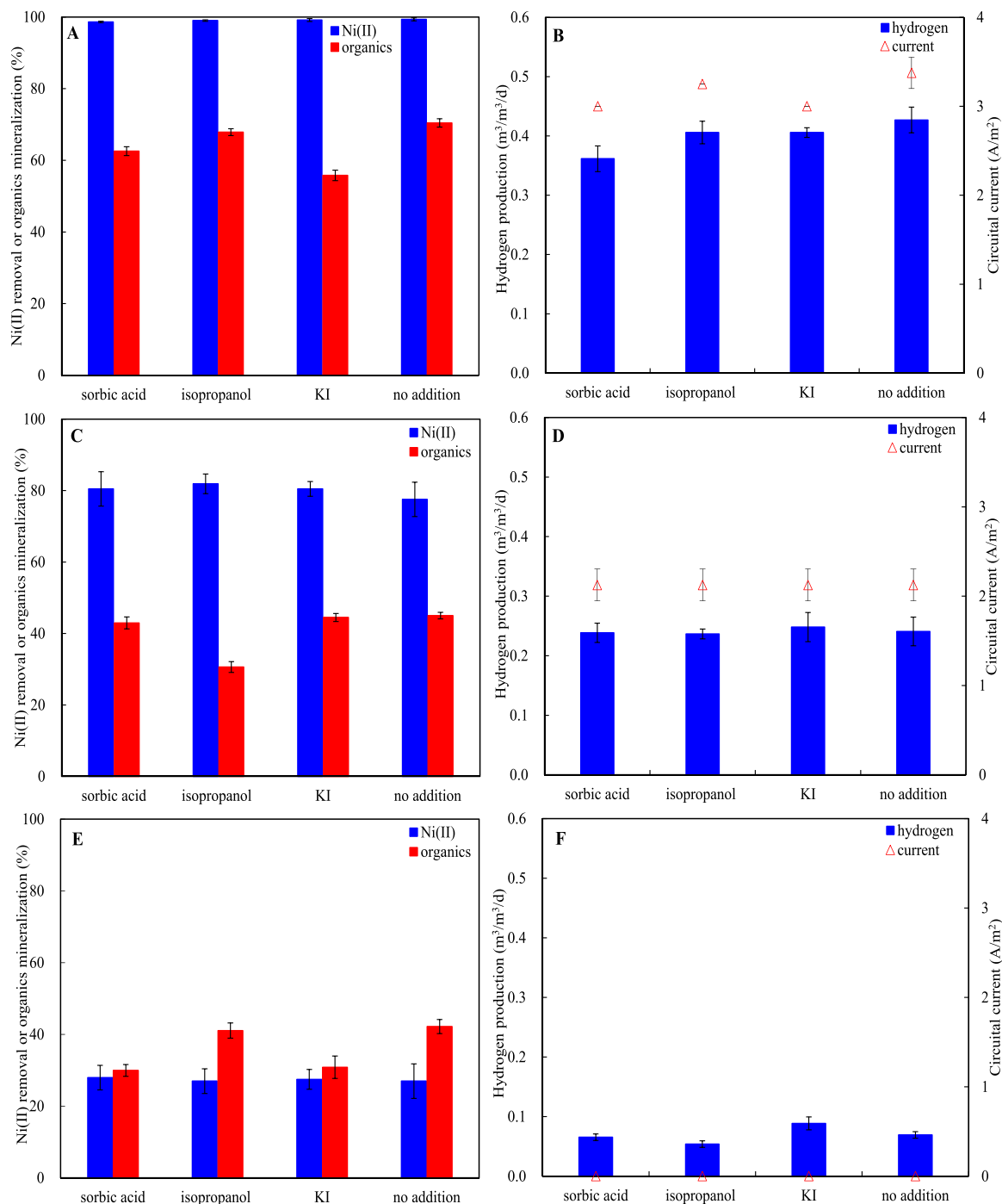
Fig. 1. Comparison of Ni(II) removal and organics mineralization (A), hydrogen production and circuital current (B), coulombic efficiencies for Ni(II) reduction (CE_{Ni}) or hydrogen evolution (CE_{H2}) (C), energy efficiencies for either Ni(II) reduction (D) or hydrogen evolution (E) and relative with considering organics ($\eta_{s,Ni}$ or $\eta_{s,H2}$, %), electrical input ($\eta_{E,Ni}$ or $\eta_{E,H2}$, %), or both electricity and organics inputs ($\eta_{s+E,Ni}$ or $\eta_{s+E,H2}$, %), and solar to hydrogen conversion efficiency (F) under various conditions (operation time: 24 h).

reflecting the significant energy conversion gain obtained with this ZnFe$_2$O$_4$/g-C$_3$N$_4$ cathode single-chamber MECs.

3.3. Possible pathways of recalcitrant organic mineralization and Ni(II) recovery

The possible pathways for the mineralization of the recalcitrant organics in the ETW were investigated by performing active species

trapping experiments to measure the main oxidative active species (Fig. 2). The introduction of the ^{3}EPS* scavenger sorbic acid or of the valence band hole scavenger KI led to significant decrease in recalcitrant organics mineralization (*p*: 0.017 ~ 0.044, Fig. 2A) and thus diminished hydrogen production and circuital current (Fig. 2A and B), whereas the introduction of isopropanol ·OH scavenger led to negligible influences (*p*: 0.238) (Fig. 2A). These results confirmed the occurrence of collaborative holes (65%) from the semiconductor ZnFe$_2$O$_4$/g-C$_3$N$_4$ cathodes

Fig. 2. Comparison of Ni(II) removal and recalcitrant organics mineralization (A, C and E), and hydrogen production and circuital current (B, D and F) in the presence of both photo irradiation and circuital current (A and B), individual circuital current (C and D) or single photo irradiation (E and F), and under conditions of different trapping agents (operational time: 24 h).

and the ^{3}EPS* (35%) derived from the exoelectrogens for efficient recalcitrant organics mineralization in the PS-MECs. Conversely, appreciable higher amount of ·OH (p: 0.014) rather than ^{3}EPS* (p: 0.389) contributed to recalcitrant organics mineralization in the control experiments with single-chamber MECs without light irradiation (Fig. 2C and D), while the dominant role of ^{3}EPS* (p: 0.038) rather than holes (p: 0.088) was observed in the single bio-light-irradiation controls (Fig. 2E and F). Collectively, these results confirmed the dominant oxidative roles of the triplet intermediates ^{3}EPS* originated from exoelectrogens, and of the holes produced by the irradiation of the ZnFe$_2$O$_4$/g-C$_3$N$_4$ cathodes, in achieving efficient mineralization of

recalcitrant organics in the ETW.

Ni(II) recovery was always ascribed to the bioelectrochemical processes due to the significant decrease observed in the absence of circuital current (Fig. 2E) and the irrelevant impact of the other operational conditions (p: 0.281 ~ 0.991) (Fig. 2A, C and E).

3.4. System performance over time

A prolonged 12-cycle operation further extended the rate of recalcitrant organics mineralization (11.3 ± 0.1 mg/L/h vs. 9.7 ± 0.2 mg/L/h, p: 0.019) (Fig. 3A) and hydrogen production (0.55 ± 0.02 m^3/m^3/
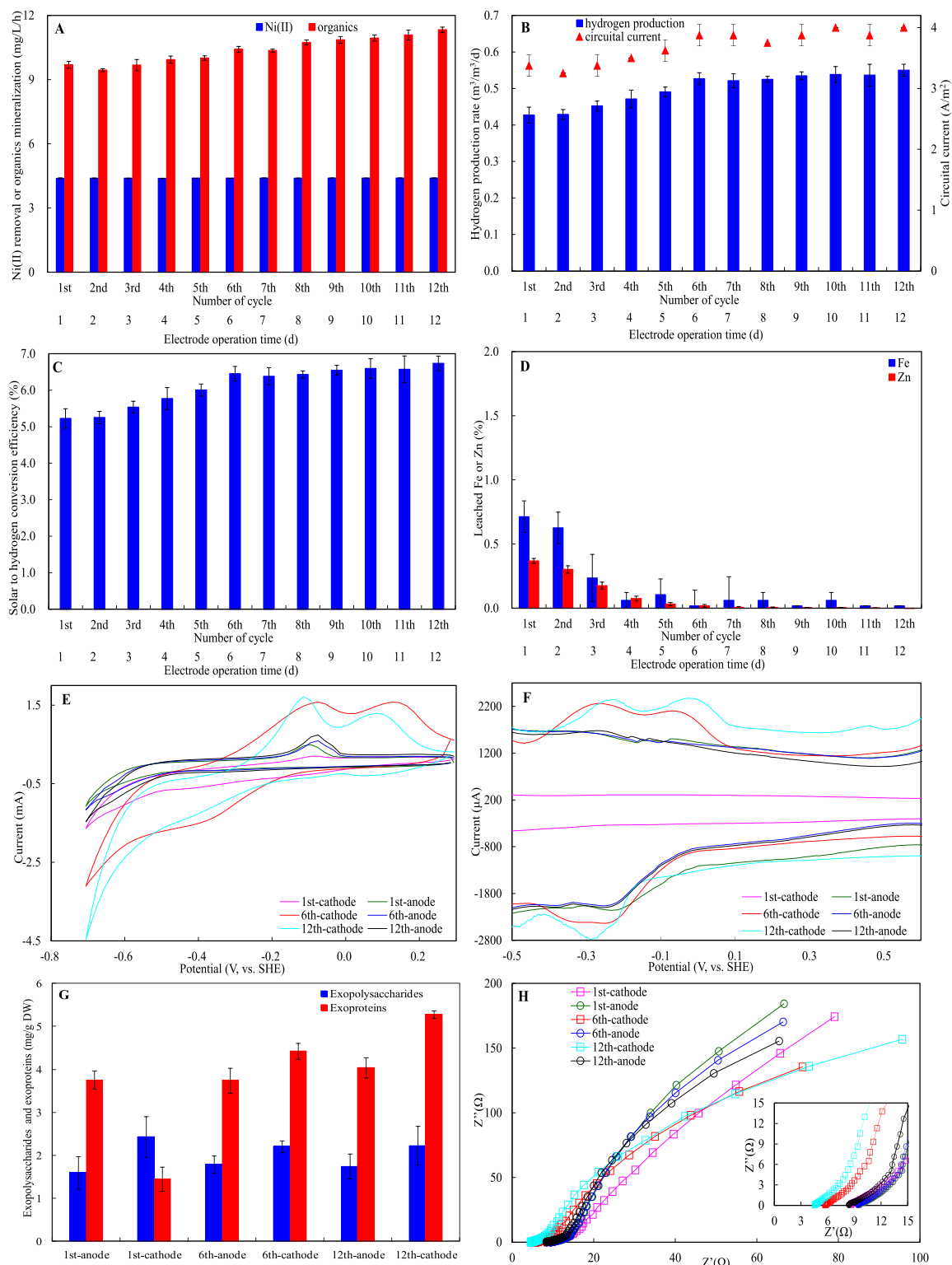
Fig. 3. Comparison of Ni(II) removal and organics mineralization (A), hydrogen production and circuital current (B), solar to hydrogen conversion efficiency (C), and leached Fe and Zn in electrolyte (D) over time. CV tests (E), differential pulse voltammetry (DPV) (F), exopolysaccharides and exoproteins (G), and EIS (H) of the cathodes and/or the anodes at the operational number of cycles of 1, 6 or 12.

d vs. 0.43 ± 0.02 m^3/m^3/d, p: 0.050) (Fig. 3B) along with appreciable higher η_L ($6.7 \pm 0.2\%$ vs. $5.3 \pm 0.3\%$, p: 0.049) (Fig. 3C), and stable Ni (II) removal (4.4 ± 0.02 mg/L/h, p: 1.00) (Fig. 3A), coulombic efficiency (p: 0.095 ~ 0.115) and energy conversion efficiency (p: 0.086 ~ 0.127) over time (Fig. S5). A smaller 6-cycle operation only improved

hydrogen production (p: 0.047) with insignificant recalcitrant organics mineralization (p: 0.089) (Fig. 3A and B). These improvements (6- or 12-cycle operations: hydrogen production; 12-cycle operation: recalcitrant organics mineralization) cannot be explained by the circuital current since the change was insignificant over time (p: 0.095 ~ 0.219)

(Fig. 3B).

The leached amount of Fe ($0.71 \pm 0.12\%$) and Zn ($0.37 \pm 0.02\%$) observed after the 1st operational cycle decreased sharply, Fe ($0.10 \pm 0.12\%$) and Zn ($0.03 \pm 0.01\%$), after the 5th-cycle (Fig. 3D) confirming the robust stability of these Fe and Zn oxides on the cathodes over time, which is an important aspect for industrial application of such system for ETW treatment.

Operation of the PS-MECs over multiple cycles (1st-cycle, 6th-cycle and 12th-cycle), gradually shifted the cathodic reductive onset potential of hydrogen evolution (-0.50 V, -0.40 V and -0.36 V) and Ni(II) reduction (-0.19 V, -0.16 V and -0.14 V) to more positive values, and the cathodic organics oxidative onset potentials to more negative values (-0.27 V, -0.42 V and -0.46 V), which accordingly exhibited gradual increases in hydrogen reductive peak currents (-1.64 mA, -3.11 mA and -4.47 mA), Ni(II) reductive peak currents (-0.61 mA vs. $-0.99 \sim -1.10$ mA), or organics oxidative peak currents (0.23 mA, 1.58 mA and 1.72 mA) (Fig. 3E; Table S4), consistent with the results in Fig. 3A and B. The more positive reductive onset potentials or negative oxidative onset potentials indicate a decrease in the corresponding thermodynamic overall free energy of the electron transfer reactions, whereas higher reductive or oxidative peak currents suggest varying degrees of the reductive or oxidative dynamic mass transfer improvements [3,38].

In contrast to the cathodic behaviors, all anodic reductive onset potentials and reductive peak potentials for hydrogen evolution and Ni (II) reduction, as well as the anodic organics oxidative onset potentials and oxidative peak potentials, remained unaltered over time, despite the small increase in hydrogen reductive peak currents (-1.07 mA, -1.16 mA and -1.47 mA), Ni(II) reductive peak currents (-0.17 mA vs. -0.21 mA), or organics oxidative peak currents (0.50 mA, 0.59 mA and 0.75 mA) (Fig. 3E; Table S4). These results in concert demonstrated the progressive modification of the physical and chemical structure of the $ZnFe_2O_4$/g-C_3N_4 cathodes over time, while the bioanodes remained relatively stable.

DPV analysis of the cathodes at the 12th-cycle operation confirmed the presence of two reduction peaks with similar reductive peak potentials (~ -0.26 V; ~ 0.02 V) and higher reduction peak currents than the 6th-cycle operation (2349 mA vs. 2261 mA; 2373 mA vs. 2102 mA), while the 1st-cycle operation did not show reduction peaks (Fig. 3F; Table S5). For the anodes, however, two reduction peak potentials of ~ -0.26 V and ~ -0.14 V with negligible changes in reduction peak currents (1624 – 1682 mA; 1444 – 1557 mA) were always observed during the 12th-cycle operation (Fig. 3F; Table S5). The reduction peak potentials at ~ 0.02 V, ~ -0.14 V and ~ -0.26 V were indicative of the use of outer membrane *c*-type cytochromes, flavins or MtrC-bound flavin, respectively as extracellular electron transfer (EET) mediators whereas the higher reduction peak current implied favorable conditions for developing a higher fraction of microbial components for mediating the EET processes [39–42]. Thus, these results might collectively indicate the likely development of a higher fraction of MtrC-bound flavin and outer membrane *c*-type cytochromes for EET in the cathodic electrotrophs over time, compared to the stable harboring of MtrC-bound flavin and flavins in the anodic exoelectrogens.

The preferential electrotrophic secretion of exoproteins (*p*: 0.001 – 0.023) over exopolysaccharides (*p*: 0.606 – 0.908) significantly increased during the 12th-cycle operation, while the exoproteins and exopolysaccharides released by the exoelectrogens remained relatively unaltered over time (Fig. 3G). Moreover, the amount of exoproteins, rather than exopolysaccharides, in both electrode biofilms was positively correlated to photo-irradiation (Fig. 3G; Fig. S6A). Considering the redox-activity of many EPS proteins with engagement in EET, and that bacterial adhesion is correlated with the amount of lipopolysaccharides [40–43], the higher fraction of exoproteins released by the electrotrophs, rather than the exoelectrogens at the 12th-cycle operation, might have been involved into the EET processes and thus accounted for the higher and predominant presence of triplet active species ^{3}EPS* (78%) rather than holes (22%) during the mineralization

of the recalcitrant organics in the ETW (Fig. S6B and C). The observable ^{3}EPS* (cathodic and anodic 78%) and holes (cathodic 22%) at the 12th-cycle operation was converse to that of cathodic holes (65%) and anodic ^{3}EPS* (35%) after the 1st-cycle operation (Fig. 2A), demonstrating the progressive temporal development of exoproteins in the electrotrophs, as the dominant reactive species for recalcitrant organics mineralization. The presence of ^{3}EPS* has very recently been observed in specific pure or mixed cultures used for recalcitrant organics degradation in other irradiated bioelectrochemical systems [18,20].

The EIS spectra after the 12th-cycle operation (Fig. 3H; Table S4) were further analyzed by fitting the spectra to an equivalent circuit (Fig. S7). The results showed that the relative importance of the resistance of the solution and the electrode (R_s), the charge transfer resistance (R_{ct}), and the diffusional resistance (R_s) of the cathodes, were all consistent with the results shown in Fig. 3E – F.

Collectively, these results have shown the impact of prolonged PS-MECs operation which resulted in the electrotrophic physiological release, on the semi-conductor $ZnFe_2O_4$/g-C_3N_4 cathodes, of EPS with higher fraction of exoproteins. Mechanistically, these phenomena, in turn, reduced the internal resistance for EET, and the simultaneous photo-induced production of excited triplet states ^{3}EPS* enhanced the mineralization of recalcitrant organics in the ETW.

### 3.5. Electrode morphology and product analysis

The morphology of the cathode electrode after the 6th- and the 12th-cycle operation is shown in Fig. 4. The cathode after 12th-cycle prolonged operation (Fig. 4A) comparatively to the 6th-cycle (Fig. 4F), was covered with a higher number of rod-shaped bacteria and with large irregular-shaped agglomerates, which were consistent with a stronger Ni signal (Fig. 4B and G; Table S6), also in comparison with the initial abiotic $ZnFeO_4$/g-C_3N_4 cathode (Fig. S2A). This result illustrated the progressive migration of bacteria towards the cathodes with progressive nickel deposition, despite that SEM alone cannot be used to exactly quantify the biomass growth over the cathode. Moreover, the EDS elemental mapping of the cathodes indicated the presence and more uniform distribution of Ni (Fig. 4C), Fe (Fig. 4D) and Zn (Fig. 4E) elements after the 12th-cycle operation in comparison to the 6th-cycle operation (Fig. 4H, I and J).

Compared to the irregular-shaped agglomerates deposited on the cathodes (Fig. 4F), the anodes exhibited uniform bacterial distribution at the same 6th-cycle operation (Fig. 4K), with the absence of any Ni signal (Fig. 4L). Such anode and cathode morphological disparities might be mainly attributed to the inherent redox circumstances, and thus different reactions and bacterial development [44] as subsequently described.

3.6. Reuse of the 6-cycle $ZnFe_2O_4$/g-C_3N_4 cathodes after calcination

The reuse of the 6-cycle $ZnFe_2O_4$/g-C_3N_4 cathodes after calcination exhibited appreciable higher photocurrent (Fig. S8A) and higher charge carrier densities (6.25×10^{22} cm^{-3} vs. 4.16×10^{22} cm^{-3}) (Fig. S8B) than the controls without calcinations or the new prepared electrodes, implying efficient electron-hole separation in the calcinated $ZnFe_2O_4$/g-C_3N_4 heterojunction due to the nickel previously deposited over 6-cycle ETW treatment. Previous results also reported that calcinations of Ni-based catalysts in pure electrochemical or photocatalytic processes resulted in enhanced performance [15,17].

After re-assembly of the 6-cycle calcined $ZnFe_2O_4$/g-C_3N_4 cathode with the corresponding bioanode, the PS-MECs achieved slightly higher recalcitrant organics mineralization (10.1 ± 0.1 mg/L/h) (Fig. 5A) and hydrogen production (0.50 ± 0.01 m^3/m^3/d) at a circuital current of 3.8 ± 0.03 mA/m^2 (Fig. 5B) than with the freshly prepared cathodes after 1st-cycle operation (Fig. 3A and B). *CE* and energy conversion efficiencies (Fig. S9) were invariably similar to those observed without recalcination (Fig. S5). A further prolonged 6-cycle operation
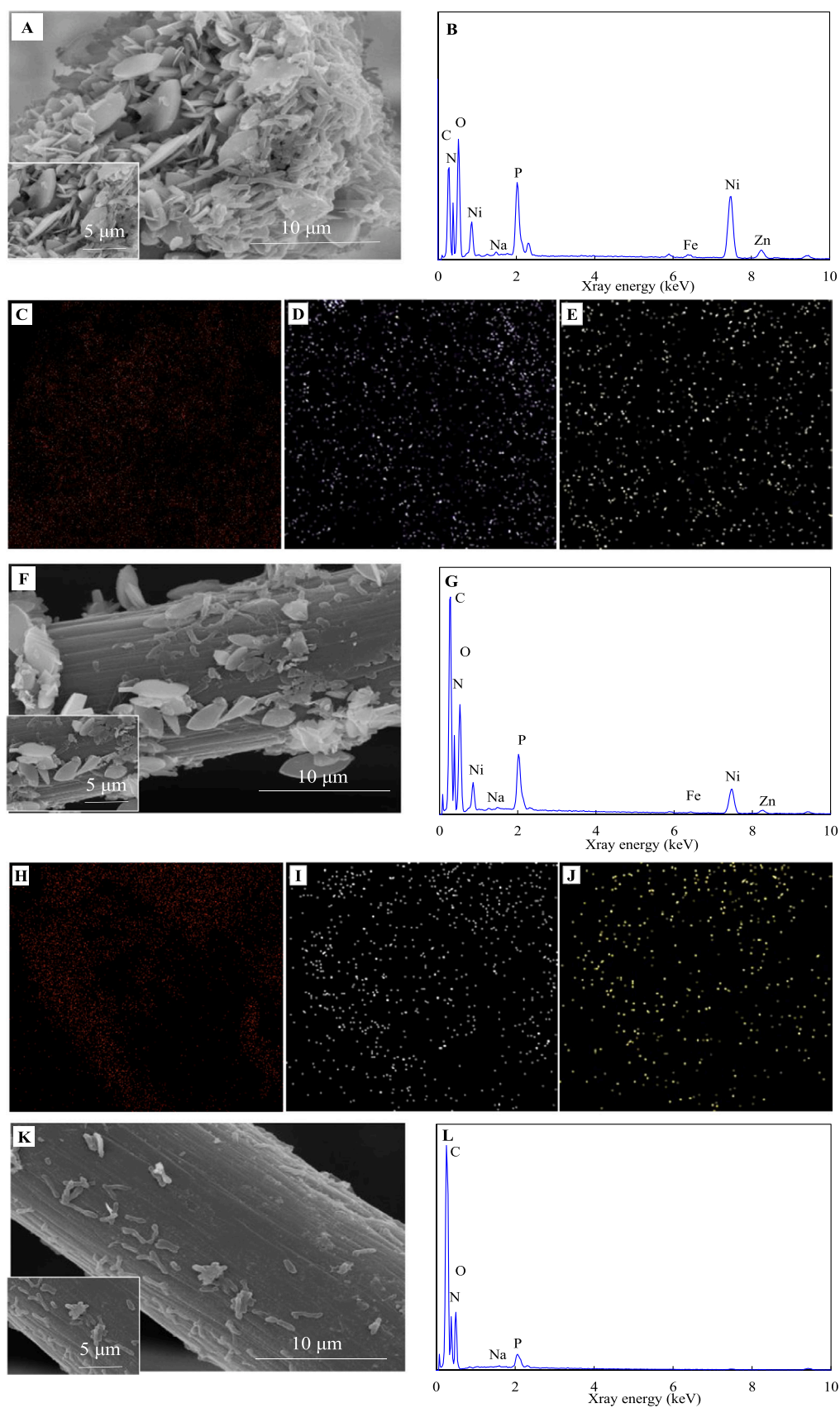
Fig. 4. Morphological SEM observation (A, F and K) and EDS determination (B, G and L) on the cathodes (A and F) or the anodes (K) at the operational number cycles of 12 (A and K) or 6 (F). EDS element mapping images of Ni (C and H), Fe (D and I) and Zn (E and J) on the cathodes at the operational cycles of 12 (C – E) or 6 (H – J).
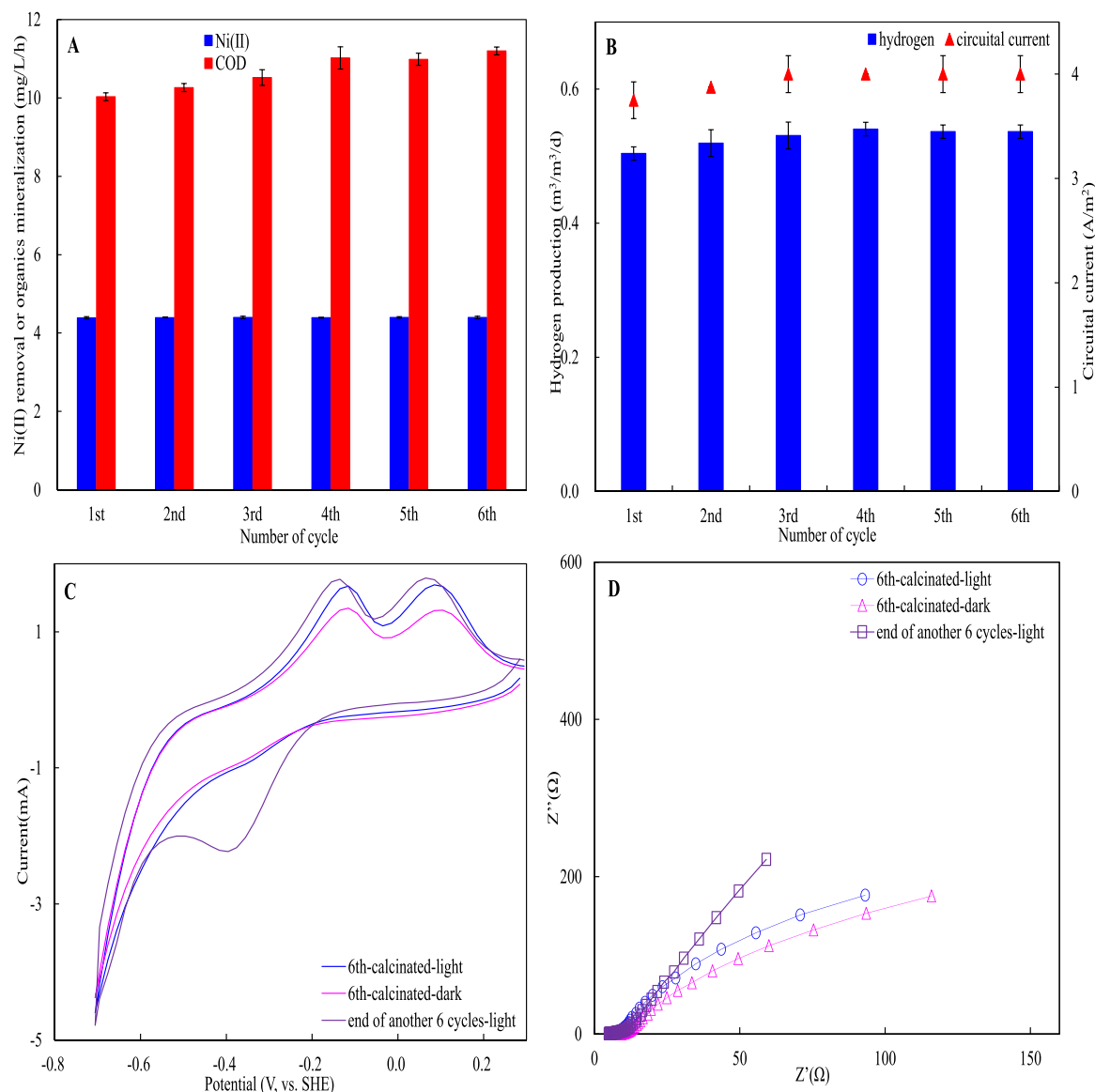
Fig. 5. Assessment of Ni(II) removal and organics mineralization (A), hydrogen production and circuital current (B), CV tests (C), and Nyquist plots of EIS spectra (D) on the calcinated $ZnFe_2O_4/g$-C_3N_4 cathodes for ETW treatment.

significantly improved recalcitrant organics mineralization (*p*: 0.016) and circuital current (*p*: 0.042) compared to the results after the 1st-cycle, but sustained similar hydrogen production (*p*: 0.106) (Fig. 5A). This was consistent with the more negative oxidative onset potential and higher oxidative peak current for recalcitrant organics, and similar reductive onset potential and reductive peak current for hydrogen evolution (Fig. 5C; Table S4), and thus smaller internal resistance (Fig. 5D; Table S4). While elemental Ni was apparently observed on the cathodes (Fig. S10A – D; Table S6), the two similar redox peaks (–0.21 V, 2191 mA; −0.06 V, 1931 mA) observed by DPV (Fig. S10E) matched those observed after the same 6th-cycle operation, but with lower currents than after the 12th-cycle operation without calcination (Fig. 3F; Table S5). The same trend with fractionally higher contribution of $^3EPS^*$ (69%) than holes (31%) for recalcitrant organics mineralization after the 6th-cycle operation (Fig. S10F and G), and the increase ($^3EPS^*$: 78%; holes: 22%) at the 12th-cycle operation without calcinations (Fig. S6B and C), reflected the collaboratively accelerated development of photo-induced $^3EPS^*$ resulting from the in-situ deposited Ni and recalcination.

3.7. Microbial community composition

The microbial community composition of the electrodes for duplicate PS-MECs experiments carried out over 12-cycles, in the presence or in the absence of light illumination was determined to understand the metabolic regulation of the main functional bacteria. A total of 107821 high-quality 16 S rRNA gene sequences were obtained from four generated libraries, with an average length of 419 nucleotides. The sequences were assigned into 836 OTUs with a distance limit of 0.03. The plateau of rarefaction curves (Fig. S11A) implied the sufficient coverage of the bacterial communities. The bacterial communities on the cathodes and on the anodes presented very little similarity, both in the presence or in the absence of light irradiation, as they were grouped in the different quadrants (Fig. 6 A). A dendrogram constructed on the base of community phylogenetic lineages further supported the dissimilarities of these bacterial communities (Fig. 6B). Moreover, the presence (cathode: 2.94; anode: 2.44) or absence (cathode: 3.68; anode: 3.57) of light irradiation greatly differentiated the diversity of the bacterial communities on both electrodes (Fig. S11B). These findings demonstrated that the composition of the bacterial communities at the anode
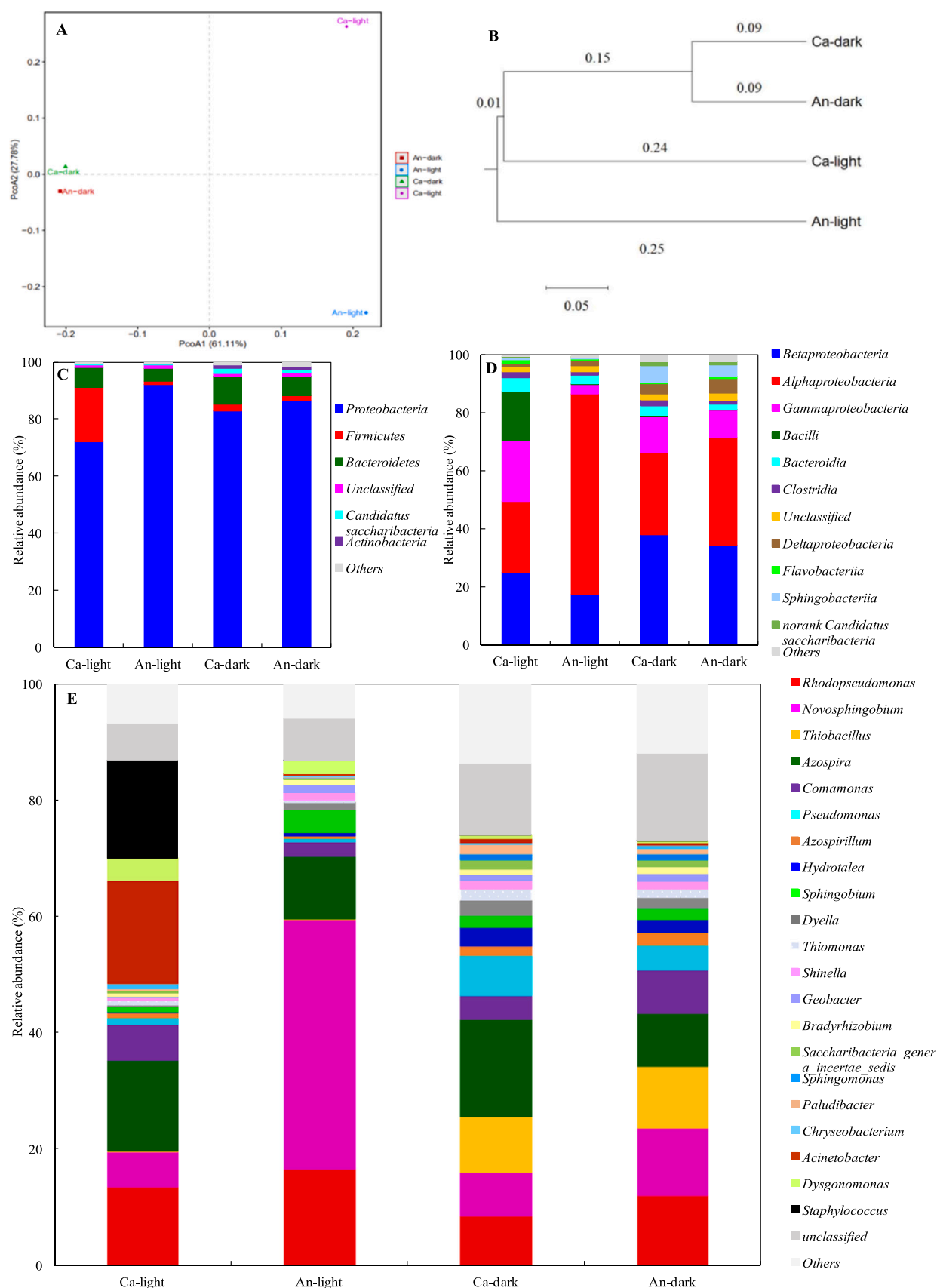
Fig. 6. Weighted Fast UniFrac (A) principle coordinates analysis and (B) cluster of the bacterial communities on the basis of phylogenetic lineages that samples contain. Comparison of relative abundance of bacterial reads retrieved from the cathodes and the anodes after a 12-cycle operation in the presence or in the absence of light irradiation and classified at (C) the phylum level, (D) the class level, or (E) the genus level distributions. Phyla, classes and genera that represent less than 1.0% of the total bacterial community composition were classified as "others".

and cathode greatly diverged and that light irradiation was highly influential on the nature of the bacterial communities, in agreement with the results in Fig. 1.

The bacterial community consisted of 6 phyla, with the major sequences (72.0 – 92.0%) belonging to *Proteobacteria* (Fig. 6 C), which has been frequently observed in pure single-chamber MECs for ETW treatment [11] and in other bioelectrochemical systems used for heavy metals recovery or recalcitrant organics degradation [1–3,26,35,44,45]. The abundance of *Firmicutes* on the cathodes (19.1%) was significantly higher than on the anodes (1.2%) under light irradiation, while it was 1.7 – 2.2% on both electrodes under darkness conditions (Fig. 6 C), or 2.8% on the initial anodes (Fig. S3A). In addition, *Actinobacteria* was absent with much less *Candidatus saccharibacteria* on both electrodes under light irradiation.

Class level characterization demonstrated the appreciable abundance of *Bacilli* on the cathodes (17.2%) with light irradiation, than 0.1 – 0.2% in all other cases (Fig. 6D; Fig. S3B). Conversely, *Alphaproteobacteria* (69.2%) was dominantly present while *Flavobacteriia* and *norank Candidatus saccharibacteria* were absent on the same anodes under light irradiation. *Sphingobacteriia* on both electrodes was flourishing over time and more apt to darkness circumstance (3.7 – 5.4% vs. 0.4 – 2.4%) (Fig. 6D; Fig. S3B).

The appreciable high abundances of *Acinetobacter* (17.7%) and *Staphylococcus* (16.8%) genera on the cathodes with light irradiation, contrasted with their nearly absence either under darkness conditions or on the anodes at the 12th-cycle operation (*Acinetobacter*: 0.3 – 0.6%; *Staphylococcus*: 0.0 – 0.1%) (Fig. 6E) or before ETW feed (*Acinetobacter*: 7.6%; *Staphylococcus*: 3.2%) (Fig. S3C). *Acinetobacter* and *Staphylococcus* genera are robust recalcitrant organics degrader and survived under the harsh ETW environment, since they are likely primary inorganic carbon fixers via the Wood-Ljungdahl pathway [44,46,47]. Along with the overwhelming predominant presence of *Novosphingobium* (42.9%) on the anodes with light irradiation, compared to its lower abundances under darkness conditions, or on the initial anodes (3.0%), and on the cathodes at the same 12th-cycle operation (6.1 – 11.5%), overall, these results demonstrated that the bacterial community compositions on both electrodes were enormously different under light irradiation. The dominant bacteria *Acinetobacter* and *Staphylococcus* on the cathodes along with the *Novosphingobium* on the anodes after 12th-cycle operation, undoubtedly path the way towards constructing efficient ZnFeO$_4$/g-C$_3$N$_4$ cathodes in PS-MECs, to achieve efficient ETW treatment in future study. In contrast, darkness conditions favored a high abundance of *Thiobacillus* (9.4 – 10.6%) homogenously distributed over both anodes and cathodes electrodes, compared to its nearly absence (~ 0.1%) under light irradiation. Similarly, genus *Rhodopseudomonas* was also universally and abundantly observed on both electrodes, but without sensitivity to light/dark conditions (cathode: 8.4 – 13.4%; anode: 12.0 – 16.5%). This genus might have contributed to the pale red electrode color observed regardless of light irradiation, consistent with other reports [35,48]. In addition, *Shinella* (0.6 – 1.5%) and *Geobacter* (0.2 – 1.3%) were always observed but with low abundance, both of which reportedly completely degraded recalcitrant organics (e.g., pyridine, aniline or azo dye) or removed many heavy metals in bioelectrochemical systems [1,3,49–51]. The genera mentioned above might have played roles as core members in randomly selected samples of both electrode biofilm well acclimated to the ETW after the 12th-cycle operation. However, it is difficult even using DNA-based stable-isotope probing techniques to directly associate the kinetics results with the activities of these specific genera [1,3,42,44]. As a compromise, clarifying cytochrome profiling of pure cultures and the specific biochemical characteristics of the pure exoelectrogens/electrotrophs maybe helpful to explain the improved rate, efficiency and yield of the system. Further studies on these genera, particularly in relation to their preference to anode/cathode or light/darkness, will help us understand the roles of these genera in the bacterial communities and thus develop efficient PS-MECs able to efficiently treat ETW. In addition, considering the

progressively observed bidirectional electron transfer processes in exoelectrogenic and electrotrophic bacteria [42,44], the simultaneous existence of the same genera on both electrodes of the ETW-fed PS-MEC might provide the source of new specific exoelectrogens and electrotrophs. Identifying the properties of these electroactive bacteria isolated under environmentally stressing conditions (e.g., carbon limitation, high salinity, low/high temperatures, and the presence of heavy metals/contaminants) and identifying their capability to drive bidirectional electron transfer processes are also highly exciting and promising aspects.

Fig. S12 shows the classification and difference of bacterial functional features on KEGG categories at levels 1 – 3. Among the 21 kinds of bacterial functions, membrane transport, cellular processes and signaling, translation, transcription, metabolism, and glycan biosynthesis and metabolism in samples of cathodes were higher than in the anodes. Conversely, the anodic cell motility, carbohydrate metabolism, and amino acid metabolism was higher than in the cathodes under the same light irradiation (Fig. S12A). The higher xenobiotics biodegradation and metabolism, and the metabolism of terpenoids and polyketides observed in samples taken from both electrodes under light irradiation rather than under darkness conditions, indicated the similar shift of these functional features of the bacterial community during the efficient mineralization of ETW recalcitrant organics in the reactors.

The level 3 pathways of the amino acid metabolism and membrane transport are shown in Fig. S12B – C. The amino acid metabolism pathways including valine, leucine and isoleucine biosynthesis, valine, leucine and isoleucine degradation, tryptophan metabolism, lysine degradation, glycine, serine and threonine metabolism, and arginine and proline metabolism in samples of anodes with light irradiation all increased (Fig. S12B). Regarding the membrane transport, the transporters and ABC transporters in samples of both electrodes were enriched by light illumination (Fig. S12C), indicating that electron transfer associated with cellular transport through the membrane was stimulated during efficient ETW treatment. Collectively, these results clearly indicate that both the shift of the microbial community composition and the metabolic regulation of these functional bacteria on both electrodes by light illumination, produced efficient activity in the PS-MECs, explaining the metabolic mechanism of efficient ETW treatment.

4. Conclusions

In this study, ZnFe$_2$O$_4$/g-C$_3$N$_4$ heterojunctions were for the first time employed as photo-assisted cathodes of single-chamber MECs together with graphite felt bioanodes to achieve efficient treatment of actual industrial ETW, simultaneous Ni(II) recovery and hydrogen production with the effluent meeting the China national discharge standards. The high solar to hydrogen conversion efficiency of 5.3% as well as the appreciably high electrical efficiency for H$_2$ production ($\eta_{E,H2} = 204\%$) exceeding 100%, firmly demonstrated the achievement of efficient energy conversion and positive energy feedback in the ETW treatment. A prolonged 12-cycle operation of the PS-MECs enhanced the rates of recalcitrant organics mineralization (11.3 mg/L/h), hydrogen production (0.55 m^3/m^3/d) and the solar to hydrogen conversion efficiency (6.7%).

While Ni(II) recovery was always ascribed to bioelectrochemical processes, its deposition over the cathode combined with the progressive electrotrophic and exoelectrogenic physiological release of EPS was found to influence the relative amount of reactive oxidative species responsible for recalcitrant organics mineralization. These species dynamically evolved during the operation of the PS-MECs, and triplet active species ^{3}EPS* (78%) rather than cathodic holes (22%) contributed to recalcitrant organics mineralization during the prolonged 12-cycle operation, while the cathodic holes (65%) were predominant over ^{3}EPS* (35%) during the 1st-cycle. The recalcination of cathodes utilized for 6 cycles exhibited appreciable higher ^{3}EPS* (69%) than holes (31%) for recalcitrant organics mineralization after another 6-

cycle operation. Collectively, these results confirmed that progressive photo-induced production of ^{3}EPS* resulting from the dynamic electrotrophic and exoelectrogenic physiological release of EPS compounded positively with the in-situ deposited Ni to achieve efficient ETW treatment.

The dynamic evolution of the PS-MECs was also confirmed by the evolution of the microbial community over the cathode and anode. The appreciable higher relative abundances of genera *Acinetobacter* (17.7%) and *Staphylococcus* (16.8%) on the cathodes, along with the overwhelming predominant *Novosphingobium* (42.9%) on the anodes of the PS-MECs after 12th-cycle operation suggested the enormous difference of bacterial community compositions on both electrodes. This along with the KEGG based PICRUSt functional prediction indicated both the shift of the microbial community composition and the metabolic regulation of the functional bacteria on both electrodes in the presence of light illumination, explaining the metabolic mechanism of efficient ETW treatment after prolonged 12-cycles operation.

In terms of economic feasibility, the cost of the cathode has been regarded to severely impede the advancements of PS-MECs due to the high-cost of noble metals with high catalytic performance [8]. The economic benefits deriving from the use of $ZnFe_2O_4/g-C_3N_4$ cathode materials ($102/m^2 see SI) in comparison for example to the MoS_2/Cu_2O cathode ($1071) [6] should further advance the practical application of PS-MECs for efficient ETW treatment, particularly when the process is combined with the concomitant recovery of added-value heavy metals.

Overall, this study contributes to the sustainable development of the electronic and semiconducting industry and broadens the application of cost-effective and efficient photo-assisted semiconducting heterojunctions cathodes in single-chamber MECs for industrial water treatment.

CRediT authorship contribution statement

Liping Huang: Conceptualization, Methodology, Investigation, Supervision, Writing – original draft. **Weifeng Kong:** Conceptualization, Methodology, Data curation. **Shiping Song:** Methodology, Data curation. **Xie Quan:** Methodology, Writing – review & editing. **Gianluca Li Puma:** Visualization, Writing – review & editing.

Declaration of Competing Interest

The authors declare that they have no known competing financial interests or personal relationships that could have appeared to influence the work reported in this paper.

Data availability

Data will be made available on request.

Acknowledgements

Appendix A. Supporting information

Supplementary data associated with this article can be found in the online version at doi:10.1016/j.apcatb.2023.122849.

References

[1] X. Dominguez-Benetton, J. Chandrakant Varia, G. Pozo, O. Modin, A. ter Heijne, J. Fransaer, K. Rabaey, Metal recovery by microbial electro-metallurgy, Prog. Mater. Sci. 94 (2018) 435–461, https://doi.org/10.1016/j.pmatsci.2018.01.007.

[2] W.F. Yan, Y. Xiao, W.D. Yan, R. Ding, S.H. Wang, F. Zhao, The effect of bioelectrochemical systems on antibiotics removal and antibiotic resistance genes: a review, Chem. Eng. J. 358 (2019) 1421–1437, https://doi.org/10.1016/j.cej.2018.10.128.

[3] M. Sun, L. Zhai, Y. Mu, H. Yu, Bioelectrochemical element conversion reactions towards generation of energy and value-added chemicals, Prog. Energy Combust. Sci. 77 (2020), 100814, https://doi.org/10.1016/j.pecs.2019.100814.

[4] H. Yu, L. Huang, G. Zhang, P. Zhou, Physiological metabolism of electrochemically active bacteria directed by combined acetate and Cd(II) in single-chamber microbial electrolysis cells, J. Hazard. Mater. 424 (2022), 127538, https://doi.org/10.1016/j.jhazmat.2021.127538.

[5] Y. Hou, Y. Gan, Z. Yu, X. Chen, L. Qian, B. Zhang, L. Huang, J. Huang, Solar promoted azo dye degradation and energy production in the bio-photoelectrochemical system with a g-C$_3$N$_4$/BiOBr heterojunction photocathode, J. Power Sources 371 (2017) 26–34, https://doi.org/10.1016/j.jpowsour.2017.10.033.

[6] Y. Jeon, J.H. Kim, K. Koo, S. Kim, A photo-assisted microbial electrolysis cell for the exclusive biohydrogen production using a MoS$_2$-coated *p*-type copper oxide, J. Power Sources 373 (2018) 79–84, https://doi.org/10.1016/j.jpowsour.2017.11.003.

[7] Y. Wang, L. Gan, Z. Liao, R. Hou, S. Zhou, L. Zhou, Y. Yuan, Self-produced biophotosensitizers enhance the degradation of organic pollutants in photo-bioelectrochemical systems, J. Hazard. Mater. 433 (2022), 128797, https://doi.org/10.1016/j.jhazmat.2022.128797.

[8] S. Cestellos-Blanco, H. Zhang, J.M. Kim, Y. Shen, P. Yang, Photosynthetic semiconductor biohybrids for solar-driven biocatalysis, Nat. Catal. 3 (2020) 245–255, https://doi.org/10.1038/s41929-020-0428-y.

[9] S. Sun, W. Kong, L. Huang, Q. Wang, G. Zhang, P. Zhou, Synergistic light irradiation and circuital current for efficient mineralization of recalcitrant organics and sequential recovery of heavy metals from etching terminal wastewater using photo-assisted bioelectrochemical systems, J. Power Sources 522 (2022), 230991, https://doi.org/10.1016/j.jpowsour.2022.230991.

[10] L. Huang, W. Kong, S. Sun, H. Wan, Y. Shi, P. Zhou, Photo-assisted self-driven bioelectrochemical systems for simultaneous enhanced treatment of etching terminal wastewater and selective recovery of heavy metals, J. Power Sources 558 (2023), 232623, https://doi.org/10.1016/j.jpowsour.2022.232623.

[11] L. Huang, H. Wan, S. Song, D. Liu, G. Li-Puma, Complete removal of heavy metals with simultaneous efficient treatment of etching terminal wastewater using scaled-up microbial electrolysis cells, Chem. Eng. J. 439 (2022), 135763, https://doi.org/10.1016/j.cej.2021.134022.

[12] Q. Wang, L. Huang, X. Quan, G. Li-Puma, Sequential anaerobic and electro-Fenton processes mediated by W and Mo oxides for degradation/mineralization of azo dye methyl orange in photo assisted microbial fuel cells, Appl. Catal. B-Environ. 245 (2019) 672–680, https://doi.org/10.1016/j.apcatb.2019.01.026.

[13] Q. Wang, Z. Cai, L. Huang, Y. Pan, X. Quan, G. Li-Puma, Intensified degradation and mineralization of antibiotic metronidazole in photo-assisted microbial fuel cells with Mo-W catalytic cathodes under anaerobic or aerobic conditions in the presence of Fe(III), Chem. Eng. J. 376 (2019) 119566, https://doi.org/10.1016/j.cej.2018.07.168.

[14] Z. Cai, L. Huang, X. Quan, Z. Zhao, Y. Shi, G. Li-Puma, Acetate production from inorganic carbon (HCO$_3^-$) in photo-assisted biocathode microbial electrosynthesis systems using WO$_3$/MoO$_3$/g-C$_3$N$_4$ heterojunctions and *Serratia marcescens* species, Appl. Catal. B-Environ. 267 (2020), 118611, https://doi.org/10.1016/j.apcatb.2020.118611.

[15] S. Vinoth, A. Pandikumar, Ni integrated S-g-C$_3$N$_4$/BiOBr based type-II heterojunction as a durable catalyst for photoelectrochemical water splitting, Renew, Energy 173 (2021) 507–519, https://doi.org/10.1016/j.renene.2021.03.121.

[16] K.Y. Kim, D.A. Moreno-Jimenez, H. Efstathiadis, Electrochemical ammonia recovery from anaerobic centrate using a nickel-functionalized activated carbon membrane electrode, Environ. Sci. Technol. 55 (2021) 7674–7680, https://doi.org/10.1021/acs.est.1c01703.

[17] Z. Wang, P. Xu, X. Yue, A. Wang, Y. Wu, X. Liu, Y. Zhang, Effect of calcination temperature on the electrochemical performance of nickel nanoparticles on carbon coated porous silicon nanospheres anode for lithium-ion batteries, Colloid Surf. A 648 (2022), 129193, https://doi.org/10.1016/j.colsurfa.2022.129193.

[18] X. Zhang, J. Li, W. Fan, M. Yao, L. Yuan, G. Sheng, Enhanced photodegradation of extracellular antibiotic resistance genes by dissolved organic matter photosensitization, Environ. Sci. Technol. 53 (2019) 10732–10740, https://doi.org/10.1021/acs.est.9b03096.

[19] H. He, F. Han, S. Sun, H. Deng, B. Huang, X. Pan, D.D. Dionysiou, Photosensitive cellular polymeric substances accelerate 17α alpha-ethinylestradiol photodegradation, Chem. Eng. J. 381 (2020), 122737, https://doi.org/10.1016/j.cej.2019.122737.

[20] M. Zhao, X. Bai, Y. Zhang, Y. Yuan, J. Sun, Enhanced photodegradation of antibiotics based on anoxygenic photosynthetic bacteria and bacterial metabolites: A sustainably green strategy for the removal of high-risk organics from secondary effluent, J. Hazard. Mater. 430 (2022), 128350, https://doi.org/10.1016/j.jhazmat.2022.128350.

[21] S. Patnaik, K.K. Das, A. Mohanty, K. Parida, Enhanced photo catalytic reduction of Cr(VI) over polymer-sensitized g-C$_3$N$_4$/ZnFe$_2$O$_4$ and its synergism with phenol

oxidation under visible light irradiation, Catal. Today 315 (2018) 52–66, https://doi.org/10.1016/j.cattod.2018.04.008.

[22] K.K. Das, S. Patnaik, S. Mansingh, A. Behera, A. Mohanty, C. Acharya, K.M. Parida, Enhanced photocatalytic activities of polypyrrole sensitized zinc ferrite/graphitic carbon nitride n-n heterojunction towards ciprofloxacin degradation, hydrogen evolution and antibacterial studies, J. Colloid Interf. Sci. 561 (2020) 551–567, https://doi.org/10.1016/j.jcis.2019.11.030.

[23] J. Jiang, X. Wang, Y. Liu, Y. Ma, T. Li, Y. Lin, T. Xie, S. Dong, Photo-fenton degradation of emerging pollutants over Fe-POM nanoparticle/porous and ultrathin g-C_3N_4 nanosheet with rich nitrogen defect: degradation mechenism, pathways, and products toxicity assessment, Appl. Catal. B-Environ. 278 (2020), 119349, https://doi.org/10.1016/j.apcatb.2020.119349.

[24] E.L. Prince, R.W. Mccabe, L.H.G. Morton, The use of ^{1}H nuclear magnetic resonance spectroscopy and gas liquid chromatography/mass spectrometry to determine the effects of fungal biodeterioration on defined synthetic metalworking fluids, Inter. Biodeterior. Biodegrad 34 (1994) 1–20, https://doi.org/10.1016/0964-8305(94)90017-5.

[25] S. Zhi and R.G. Burns, Depolymerisation and biodegradation of a synthetic tanning agent by activated sludges, the bacteria Arthrobacter globiformis and Comamonas testosteroni, and the fungus Cunninghamella polymorpha, Biodegradation 16 (2005) 305−318, https://doi.org/10.1007/s10532−004-1723-z.

[26] L. Huang, L. Gan, N. Wang, X. Quan, B.E. Logan, G. Chen, Mineralization of pentachlorophenol with enhanced degradation and power generation from air cathode microbial fuel cells, Biotechnol. Bioeng. 109 (2012) 2211–2221, https://doi.org/10.1002/bit.24489.

[27] Q. Wang, L. Huang, H. Yu, X. Quan, Y. Li, G. Fan, L. Li, Assessment of five different cathode materials for Co(II) reduction with simultaneous hydrogen evolution in microbial electrolysis cells, Inter. J. Hydrog. Energy 40 (2015) 184–196, https://doi.org/10.1016/j.ijhydene.2014.11.014.

[28] L. Huang, Y. Liu, L. Yu, X. Quan, G. Chen, A new clean approach for production of cobalt dihydroxide from aqueous Co(II) using oxygen-reducing biocathode microbial fuel cells, J. Clean. Prod. 86 (2015) 441–446, https://doi.org/10.1016/j.jclepro.2014.08.018.

[29] W. Kong, L. Huang, X. Quan, Z. Zhao, G. Li-Puma, Efficient production of acetate from inorganic carbon (HCO_3^-) in microbial electrosynthesis systems incorporating Ag_3PO_4/g-C_3N_4 anaerobic photo-assisted biocathodes, Appl. Catal. B-Environ. 284 (2021), 119696, https://doi.org/10.1016/j.apcatb.2020.119696.

[30] S. Wang, L. Huang, L. Gan, X. Quan, N. Li, G. Chen, L. Lu, D. Xing, F. Yang, Combined effects of enrichment procedure and non-fermentable or fermentable co-substrate on performance and bacterial community for pentachlorophenol degradation in microbial fuel cells, Bioresour. Technol. 120 (2012) 120–126, https://doi.org/10.1016/j.biortech.2012.06.022.

[31] L. Huang, Z. Xu, Y. Shi, Y. Zhang, G. Li-Puma, Cellular electron transfer in anaerobic photo-assisted biocathode microbial electrosynthesis systems for acetate production from inorganic carbon (HCO_3^-), Chem. Eng. J. 431 (2022) 134022, https://doi.org/10.1016/j.cej.2021.134022.

[32] S. Suzanne Nielsen, Phenol-sulfuric acid method for total carbohydrates, Food Analysis Laboratory Manual, Springer, pp. 47−53, 2009.

[33] A. Okamoto, K. Hashimoto, K.H. Nealson, R. Nakamura, Rate enhancement of bacterial extracellular electron transport involves bound flavin semiquinones, Proc. Natl. Acad. Sci. USA 110 (2013) 7856−7861, https://doi.org/10.1073/pnas.1220823110.

[34] Y. Chen, J. Shen, L. Huang, Y. Pan, X. Quan, Enhanced Cd(II) removal with simultaneous hydrogen production in biocathode microbial electrolysis cells in the presence of acetate or $NaHCO_3$, Int. J. Hydrog. Energy 41 (2016) 13368–13379, https://doi.org/10.1016/j.ijhydene.2016.06.200.

[35] S. Song, L. Huang, P. Zhou, Efficient H_2 production in a $ZnFe_2O_4$/g-C_3N_4 photo-cathode single-chamber microbial electrolysis cell, Appl. Microbiol. Biotechnol. 107 (2023) 391–404, https://doi.org/10.1007/s00253-022-12293-3.

[36] L. Lu, F.L. Lobo, D. Xing, Z.J. Ren, Active harvesting enhances energy recovery and function of electroactive microbiomes in microbial fuel cells, Appl. Energy 247 (2019) 492–502, https://doi.org/10.1016/j.apenergy.2019.04.074.

[37] H. Luo, G. Liu, R. Zhang, Y. Bai, S. Fu, Y. Hou, Heavy metal recovery combined with H_2 production from artificial acid mine drainage using the microbial electrolysis cell, J. Hazard. Mater. 270 (2014) 153–159, https://doi.org/10.1016/j.jhazmat.2014.01.050.

[38] Z. He, F. Mansfeld, Exploring the use of electrochemical impedance spectroscopy (EIS) in microbial fuel cell studies, Energy Environ. Sci. 2 (2009) 215–219, https://doi.org/10.1039/B814914C.

[39] R. Wu, C. Wang, J. Shen, F. Zhao, A role for biosynthetic CdS quantum dots in extracellular electron transfer of *Saccharomyces cerevisiae*, Process Biochem 50 (2017) 2061–2065, https://doi.org/10.1016/j.procbio.2015.10.005.

[40] Y. Xiao, F. Zhao, Electrochemical roles of extracellular polymeric substances in biofilms, Curr. Opin. Electrochem 4 (2017) 206–211, https://doi.org/10.1016/j.coelec.2017.09.016.

[41] H. Yu, Molecular insights into extracellular polymeric substances in activated sludge, Environ. Sci. Technol. 54 (2020) 7742–7750, https://doi.org/10.1021/acs.est.0c00850.

[42] L. Huang, G. Li-Puma, Physiological response of electroactive bacteria via secretion of extracellular polymeric substances in microbial electrochemical processes: a review, Curr. Opin. Electrochem 36 (2022), 101168, https://doi.org/10.1016/j.coelec.2022.101168.

[43] X. Chen, Y. Li, J. Wu, N. Li, W. He, Y. Feng, J. Liu, Heterogeneous structure regulated by selection pressure on bacterial adhesion optimized the viability stratification structure of electroactive biofilms, ACS Appl. Mater. Inter. 14 (2022) 2754–2767, https://doi.org/10.1021/acsami.1c19767.

[44] L. Huang, X. Xing, P. Zhou, G. Li-Puma, Mixotrophic bacteria for environmental detoxification of contaminated waste and wastewater, Appl. Microbiol. Biotechnol. 105 (2021) 6627–6648, https://doi.org/10.1007/s00253-021-11514-5.

[45] W. Yan, Y. Guo, Y. Xiao, S. Wang, R. Ding, J. Jiang, H. Gang, H. Wang, J. Yang, F. Zhao, The changes of bacterial communities and antibiotic resistance genes in microbial fuel cells during long-term oxytetracycline processing, Water Res 142 (2018) 105–114, https://doi.org/10.1016/j.watres.2018.05.047.

[46] E.V. LaBelle, C.W. Marshall, H.D. May, Microbiome for the electrosynthesis of chemicals from carbon dioxide, Acc. Chem. Res 53 (2020) 62–71, https://doi.org/10.1021/acs.accounts.9b00522.

[47] M.L. Goñi, N.A. Gañán, R.E. Martini, Supercritical CO_2-assisted dyeing and functionalization of polymeric materials: A review of recent advances (2015−2020), J. CO_2 Util. 54 (2021), 101760, https://doi.org/10.1016/j.jcou.2021.101760.

[48] M. Sui, Y. Li, Y. Jiang, Y. Zhang, L. Wang, W. Zhang, X. Wang, Light exposure interferes with electroactive biofilm enrichment and reduces extracellular electron transfer efficiency, Water Res 188 (2021), 116512, https://doi.org/10.1016/j.watres.2020.116512.

[49] Y. Wang, Y. Pan, T. Zhu, A. Wang, Y. Lu, L. Lv, K. Zhang, Z. Li, Enhanced performance and microbial community analysis of bioelectrochemical system integrated with bio-contact oxidation reactor for treatment of wastewater containing azo dye, Sci. Total Environ. 634 (2018) 616−627, https://doi.org/10.1016/j. scitotenv.2018.03.346.

[50] C. Zhang, H. Chen, G. Xue, Y. Liu, S. Chen, C. Jia, A critical review of the aniline transformation fate in azo dye wastewater treatment, J. Clean. Prod. 321 (2021), 128971, https://doi.org/10.1016/j.jclepro.2021.128971.

[51] N. Bolan, M. Kumar, E. Singh, A. Kumar, L. Singh, S. Kumar, S. Keerthanan, S. A. Hoang, A. El-Naggar, A. Vithanage, B. Sarkar, H. Wijesekara, S. Diyabalanage, P. Sooriyakumar, A. Vinu, H. Wang, M.B. Kirkham, S.M. Shaheen, J. Rinklebe, K.H. M. Siddique, Antimony contamination and its risk management in complex environmental settings: A review, Environ. Inter. 158 (2022), 106908, https://doi.org/10.1016/j.envint.2021.106908.